



Published in final edited form as:

IEEE Trans Med Imaging. 2017 February ; 36(2): 641–652. doi:10.1109/TMI.2016.2623745.

A Biomechanical Modeling Guided CBCT Estimation Technique

You Zhang, Joubin Nasehi Tehrani, and Jing Wang

Department of Radiation Oncology, UT Southwestern Medical Center at Dallas, Dallas, TX 75390
USA

Abstract

Two-dimensional-to-three-dimensional (2D-3D) deformation has emerged as a new technique to estimate cone-beam computed tomography (CBCT) images. The technique is based on deforming a prior high-quality 3D CT/CBCT image to form a new CBCT image, guided by limited-view 2D projections. The accuracy of this intensity-based technique, however, is often limited in low-contrast image regions with subtle intensity differences. The solved deformation vector fields (DVs) can also be biomechanically unrealistic. To address these problems, we have developed a biomechanical modeling guided CBCT estimation technique (Bio-CBCT-est) by combining 2D-3D deformation with finite element analysis (FEA)-based biomechanical modeling of anatomical structures. Specifically, Bio-CBCT-est first extracts the 2D-3D deformation-generated displacement vectors at the high-contrast anatomical structure boundaries. The extracted surface deformation fields are subsequently used as the boundary conditions to drive structure-based FEA to correct and fine-tune the overall deformation fields, especially those at low-contrast regions within the structure. The resulting FEA-corrected deformation fields are then fed back into 2D-3D deformation to form an iterative loop, combining the benefits of intensity-based deformation and biomechanical modeling for CBCT estimation. Using eleven lung cancer patient cases, the accuracy of the Bio-CBCT-est technique has been compared to that of the 2D-3D deformation technique and the traditional CBCT reconstruction techniques. The accuracy was evaluated in the image domain, and also in the DVF domain through clinician-tracked lung landmarks.

Index Terms

Cone-beam Computed Tomography; Image Estimation; 2D-3D Deformation; Biomechanical Modeling; Finite Element Analysis; Boundary Condition; Mooney-Rivlin Material

I. Introduction

CBCT imaging is currently used in routine clinical practice for image-guided radiation therapy [1]. However, frequent imaging required by daily treatments exposes patients to additional radiation doses, increasing the risk of secondary cancers [2]. A new deformation-driven CBCT estimation approach has recently been investigated. Instead of directly reconstructing the CBCT volume from 2D projections, this approach estimates the new CBCT through deforming a previously acquired high-quality CT/CBCT image [3]–[11]. Deformation of the 3D image is guided by the acquired 2D projections (2D-3D deformation). With the high-quality image as prior information, the CBCT imaging dose can be substantially reduced by acquiring fewer projections for image estimation. The

deformation approach can also pass along the accurate Hounsfield units (HU) from high-quality prior CT images to estimated CBCT images, enabling more accurate dose calculations for radiation therapy [12]. The solved deformation field can also be utilized for tumor tracking [13], dose accumulation [14], adaptive radiation therapy [15], and functional imaging [16].

Currently available 2D-3D deformation techniques are purely intensity-based, aiming to match the intensity maps between the acquired projections and the computed projections from the deformed CBCT images. This approach usually works well for high-contrast regions [4], [6], [7] but its accuracy is often limited in low-contrast regions with subtle intensity differences [5]. In addition, the solved deformation fields may not be biomechanically realistic because the deformation fails to consider the elastic properties of anatomical structures [17].

Recently, there has been growing interest to solve image deformation problems through a biomechanical modeling-based approach [17]–[26]. Compared with the intensity-based approach, biomechanical modeling incorporates the morphology, the material composition, and the tissue elasticity of anatomical structures into the deformation process. The resulting deformation field is thus more physiologically and physically meaningful [22]. In addition, by using biomechanical modeling the whole deformation field can be computed from the provided boundary conditions, potentially generating a more accurate deformation field in low contrast regions within the anatomical structures [21].

In this study, we have developed a biomechanical modeling guided CBCT estimation technique (Bio-CBCT-est), which combines the intensity-based 2D-3D deformation technique with the finite element analysis (FEA)-based biomechanical modeling technique. The Bio-CBCT-est technique uses the accurate deformation field at high-contrast regions generated from 2D-3D deformation to correct and fine-tune the overall deformation field through biomechanical modeling, especially the deformation around low-contrast regions. Using Bio-CBCT-est, the overall physiological and physical plausibility of the derived deformation field also benefits from the correction by biomechanical modeling.

In this study, Bio-CBCT-est has been applied to estimate lung CBCT images. Based on eleven lung cancer patient cases, cone-beam projections with various sampling sparseness and noise levels were simulated for CBCT estimation, to evaluate the robustness and dose reduction potential of the Bio-CBCT-est technique. The estimation accuracy of the Bio-CBCT-est technique was compared to that of the 2D-3D deformation technique, both through the image domain and through the deformation field domain. The accuracy of the Bio-CBCT-est technique was also compared to that of the traditional Feldkamp–Davis–Kress (FDK) [27] algorithm and the total variation-regularized algebraic reconstruction technique (ART-TV) [28].

II. Materials and methods

Since 2D-3D deformation works well at high-contrast regions [4], [6], [7], Bio-CBCT-est extracts the deformation field generated by 2D-3D deformation at high-contrast structure

boundaries. Bio-CBCT-est then uses the extracted field as the boundary condition to drive FEA to optimize the deformation field within the structure boundaries. The optimized deformation field is then fed back into the 2D-3D deformation as a new starting point for further optimization, forming a loop to iteratively fine-tune the overall deformation field for CBCT estimation. Details of the 2D-3D deformation technique, biomechanical modeling of the lungs, and the overall work-flow of Bio-CBCT-est are described below:

A. The 2D-3D deformation technique

1) General form of the 2D-3D deformation technique—By 2D-3D deformation, the new $CBCT(\mu)$ is morphed from a previously acquired high-quality CT/CBCT image (μ_{prior}), through using the deformation vector field (DVF, denoted by \mathbf{v} , $\mathbf{v} \in \mathbf{R}^3$):

$$\mu(\mathbf{x}) = \mu_{prior}(\mathbf{x} + \mathbf{v}) \quad (1)$$

\mathbf{x} denotes the voxel grids of the new CBCT. As shown on the right side of the equation, the DVF \mathbf{v} is defined on the new $CBCT$ image voxel grids and points to μ_{prior} [29]. The free-form deformation [30] in (1) is driven by the tri-linear interpolation process [6]. Through (1), the problem of solving μ has been converted into that of solving \mathbf{v} .

The solution of \mathbf{v} is subjected to the following data fidelity constraint: the computed projections from μ should match the acquired projections. The corresponding equation is as follows:

$$\mathcal{A}\mu(\mathbf{x}) = \mathcal{A}\mu_{prior}(\mathbf{x} + \mathbf{v}) = P \quad (2)$$

The \mathcal{A} symbol denotes the projection computation matrix, which is in correspondence with the acquired projections P . As illustrated in (2), the process of 2D projection matching drives the deformation of the 3D volume. Thus the image estimation process is named ‘2D-3D deformation’. To enforce the data fidelity constraint of (2), we use the sum of squared differences as the image similarity metric. Thus solving (2) translates into optimizing an objective function to solve \mathbf{v} :

$$\begin{aligned} \mathbf{v} &= \underset{\mathbf{v}}{\operatorname{argmin}} f(\mathbf{v}) \\ &= \underset{\mathbf{v}}{\operatorname{argmin}} \left[\|\mathcal{A}\mu_{prior}(\mathbf{x} + \mathbf{v}) - P\|_2^2 \right] \end{aligned} \quad (3)$$

When limited-view projections are used as P , (3) presents an ill-posed problem. To further regularize the optimization problem for a stable solution [6], [7], an additional deformation energy term is defined and shown in (4):

$$E(\mathbf{v}) = \sum_{x=1}^{n_i} X \sum_{y=1}^{n_j} \sum_{z=1}^{n_k} \sum_{m=x,y,z} \left(\left(\frac{\partial v_m}{\partial x} \right)^2 + \left(\frac{\partial v_m}{\partial y} \right)^2 + \left(\frac{\partial v_m}{\partial z} \right)^2 \right) \quad (4)$$

The m parameter separates the DVF \mathbf{v} into three canonical directions x , y and z . The symbols n_x , n_y and n_z denote the DVF sizes along the three directions, respectively. The $E(\mathbf{v})$ term functions as a penalty for large variations in the DVF. Reducing $E(\mathbf{v})$ will smooth the DVF and reduce its solution space for faster and stable convergence. Adding the deformation energy term to the original objective function, turns the objective function into:

$$\mathbf{v} = \operatorname{argmin}_{\mathbf{v}} \left[\|\mathcal{A} \mu_{\text{prior}}(\mathbf{x} + \mathbf{v}) - P\|_2^2 + \omega * E(\mathbf{v}) \right] \quad (5)$$

The ω parameter denotes the weighting factor balancing the data fidelity term and the deformation energy term, which is empirically set as 0.05 in this study.

2) Solving the inverse deformation field—As shown in (1), the DVF \mathbf{v} is defined on the voxel grids of the new *CBCT* (we call it the ‘forward DVF’). However, in this study, we are using the prior image μ_{prior} for biomechanical modeling purposes. The DVF used as the boundary condition for biomechanical modeling should be defined on the prior image voxel grids. We call the corresponding DVF inverse DVF ($\mathbf{v}_{\text{inverse}}$), which is defined on the voxel grids of the prior image and points to the new *CBCT*.

Deriving the inverse DVF directly from the forward DVF is usually subjected to errors with inverse consistency [31]. To address this problem, we take a symmetric 2D-3D deformation approach to solve both the forward and the inverse DVFs simultaneously, formulated as (6):

$$\mathbf{v} = \operatorname{argmin}_{\mathbf{v}} \left\{ \|\mathcal{A} \mu_{\text{prior}}(\mathbf{x} + \mathbf{v}) - P\|_2^2 + \|\mathcal{A}_{\text{prior}} [(\mu_{\text{prior}}(\mathbf{x} + \mathbf{v})) (\mathbf{x} + \mathbf{v}_{\text{inverse}})] - P_{\text{prior}}\|_2^2 + \omega/2 * E(\mathbf{v}) + \omega/2 * E(\mathbf{v}_{\text{inverse}}) \right\} \quad (6)$$

The $\mathcal{A}_{\text{prior}}$ symbol denotes the projection computation matrix corresponding to P_{prior} . P_{prior} denotes the projections simulated from the prior image μ_{prior} . For symmetry and simplicity, we choose $\mathcal{A}_{\text{prior}} = \mathcal{A}$. The symmetric data fidelity and deformation energy terms in (6) are enforced to optimize the inverse-consistency [31] of the deformation fields, to allow the deformation results to be consistent along both forward and inverse directions. The inverse DVF $\mathbf{v}_{\text{inverse}}$ can be computed from \mathbf{v} by multiple approaches ([32]–[34]). In this study we take a simple and fast approach by setting $\mathbf{v}_{\text{inverse}} = -\mathbf{v}$.

The gradient of (6) can be explicitly computed in a similar way to that shown in [6], enabling the objective function to be minimized through the nonlinear conjugate gradient algorithm. We set the initial DVF as 0 for the optimization to start. For the implementation details of the conjugate gradient algorithm and a corresponding pseudo-code, please refer to our previous publication [7].

Based on the derived forward and inverse deformation fields, biomechanical modeling of the structures (lung) can be performed as follows.

B. Biomechanical modeling of lung

Biomechanical modeling divides the whole complex lung structure into small connected elements. Lung deformation can thus be modeled as the reactions of these elements to external boundary conditions, considering their morphological and elastic properties.

1) The theory of lung biomechanical modeling—In this study, the lung is modeled as the homogeneous, isotropic, and hyper-elastic Mooney-Rivlin [35] material. The Mooney-Rivlin material is often used to model biological soft tissues with relatively large deformations, characterized by a nonlinear stress (force)-strain (deformation) relationship. It was previously used in lung biomechanical modeling and achieved encouraging results [17] with an accuracy similar to those reported by other lung biomechanical modeling studies [19], [20], [26].

In detail, the deformation gradient tensor (\mathbf{F}) of the material can be expressed as:

$$\mathbf{F} = \begin{bmatrix} 1 + \frac{\partial v_x}{\partial x} & \frac{\partial v_x}{\partial y} & \frac{\partial v_x}{\partial z} \\ \frac{\partial v_y}{\partial x} & 1 + \frac{\partial v_y}{\partial y} & \frac{\partial v_y}{\partial z} \\ \frac{\partial v_z}{\partial x} & \frac{\partial v_z}{\partial y} & 1 + \frac{\partial v_z}{\partial z} \end{bmatrix} \quad (7)$$

v_x , v_y and v_z are the displacement components of the DVF ($\mathbf{v}_{inverse}$ as in this study) along x , y , and z directions, respectively. The left Cauchy-Green deformation tensor \mathbf{B} can be written as:

$$\mathbf{B} = \mathbf{F} \mathbf{F}^T \quad (8)$$

The \mathbf{F}^T symbol denotes the transpose of the deformation gradient tensor \mathbf{F} . The corresponding invariants of \mathbf{B} are:

$$\tilde{I}_1 = J^{-2/3} \text{tr } \mathbf{B} = J^{-2/3} (\lambda_1^2 + \lambda_2^2 + \lambda_3^2) \quad (9)$$

$$\begin{aligned} \tilde{I}_2 &= \frac{1}{2} J^{-4/3} ((\text{tr } \mathbf{B})^2 - \text{tr } \mathbf{B}^2) \\ &= J^{-4/3} (\lambda_1^2 \lambda_2^2 + \lambda_2^2 \lambda_3^2 + \lambda_1^2 \lambda_3^2) \end{aligned} \quad (10)$$

\tilde{I}_1 and \tilde{I}_2 denote the first and second invariants of \mathbf{B} , respectively. The J symbol denotes the determinant of \mathbf{F} . $\text{tr}(\ast)$ calculates the matrix trace. λ_1^2 , λ_2^2 and λ_3^2 denote the eigenvalues (principal stretches) of \mathbf{B} .

The strain energy density function (SE) of the Mooney-Rivlin material, which represents the stored energy in the material from deformation, can finally be described as a combination of three separate terms:

$$SE = c_1 (\tilde{I}_1 - 3) + c_2 (\tilde{I}_2 - 3) + 0.5K * (J - 1)^2 \quad (11)$$

The first and second terms denote the deviatoric strain energy, determining how the material shape changes in response to stress. The third term denotes the volumetric strain energy, determining how the material volume changes in response to stress. The c_1 and c_2 parameters denote the corresponding material constants for \tilde{I}_1 and \tilde{I}_2 . The K parameter denotes the bulk modulus. The c_1 , c_2 , and K parameters are related to the Young's modulus (E_Y) and the Poisson's ratio (ν_p) [17] by (12) and (13):

$$c_1 + c_2 = \frac{E_Y}{4(1 + \nu_p)} \quad (12)$$

$$K = \frac{E_Y}{3(1 - 2\nu_p)} \quad (13)$$

In this study, we model the lung as composed of homogeneous material and use the displacement vector fields at the lung surface to drive FEA. We are only interested in the solved lung displacement fields, not in the corresponding lung stress. As a result, the value of the Young's modulus E_Y is essentially irrelevant [18], [36], [37]. Thus the absolute values of $(c_1 + c_2)$ and K are not important. Dividing (13) by (12), we eliminate E_Y from the equation:

$$\frac{K}{c_1 + c_2} = \frac{4(1 + \nu_p)}{3(1 - 2\nu_p)} \quad (14)$$

To simplify the analysis, we set $c_1 = c_2 = c$ in this study. Thus (14) is further simplified as:

$$\frac{K}{c} = \frac{K}{c} = \frac{4(1 + \nu_p)}{\frac{3}{2}(1 - 2\nu_p)} = \frac{8(1 + \nu_p)}{3(1 - 2\nu_p)} = k f \quad (15)$$

After simplification, the number of parameters to optimize is essentially reduced to one, the k_factor $k f$. As shown in (15), $k f$ is correlated with the Poisson's ratio ν_p and represents the material incompressibility. Previous studies have used various ν_p values for the lung, ranging from 0.2 to 0.499 [18]–[20], [26], [38]. The corresponding range of $k f$ is around 5 to 2000. We performed a parameterized study for different $k f$ values and found that using $k f = 200$ provided the best results overall (supplementary materials are available in the supplementary files/multimedia tab). In this study, for the purpose of running FEA, we choose $c_1 = c_2 = 0.135 \text{ kPa}$ as previously described [17]. The corresponding bulk modulus is $K = c_1 * k f = 0.135 \text{ kPa} * 200 = 27 \text{ kPa}$.

In summary, with the nonlinear elastic properties of the lung material specified by the strain energy function in (11), FEA can be performed to solve the lung deformation fields from boundary conditions.

2) The implementation of lung biomechanical modeling—Lung biomechanical modeling can be performed in four steps:

1. **LUNG SEGMENTATION.** In this study, the lung is semi-automatically segmented using the ITK-SNAP software [39]. An intensity threshold (-250 HU) is first applied on the prior image μ_{prior} through ITK-SNAP to select the region of interest (ROI). Automatic lung segmentation based on the level-set method is subsequently performed within the ROI. The automatic segmentation is manually fine-tuned as the last step to correct small residual errors. The resulting final lung segmentation is converted into a binary mask to represent the spatial domain of the lung.
2. **LUNG TETRAHEDRAL MESH GENERATION.** From the lung binary mask, the lung tetrahedral mesh is generated based on the Iso2Mesh package [40] to divide the lung into small connected tetrahedron elements. A coarse surface mesh made of triangles is first generated from the lung binary mask. The coarse surface mesh then undergoes subsequent automatic check and repair to remove non-manifold vertices, including the isolated ones. Laplacian smoothing is further applied to smooth and regularize the mesh surface. Based on the repaired and smoothed mesh surface, a high-quality volumetric mesh is generated by Tetgen [41] to discretize the surface-enclosed region into small connected tetrahedron elements. The four vertices (nodes) of each tetrahedron element are checked and re-oriented for consistency so that the determinant of the Jacobian matrix corresponding to the orientation is positive [22].
3. **BOUNDARY CONDITION EXTRACTION.** The boundary condition is defined as the displacement vector of the tetrahedron nodes residing at the mesh surface (surface nodes). Based on its location in 3D space, each surface node is paired with its corresponding image voxel through the nearest neighbor matching. The displacement vector of each surface node is extracted as the displacement vector of its matching image voxel from the inverse DVF $\mathbf{v}_{inverse}$ which is solved by the 2D-3D deformation technique (6).
4. **FEA-BASED BIOMECHANICAL MODELING.** The biomechanical lung DVF is derived from the combination of the tetrahedral mesh, the extracted boundary condition and the Mooney-Rivlin hyper-elastic material modeling. In this study, the FEBio package [42] is used to perform the final finite element analysis to solve the lung biomechanical DVF.

C. The Bio-CBCT-est workflow

The full, detailed work-flow of the Bio-CBCT-est technique is shown in Figure 1.

For step 4, the lung biomechanical DVF is defined on the nodes of the tetrahedral mesh. In contrast, the intensity-based $v_{inverse}$ is defined on the voxel grids of the prior image. To merge the two DVFs, we have to convert the lung biomechanical DVF so that it is defined on the prior image voxel grids.

To address this need, the barycentric coordinates [43] of each prior image voxel are computed with reference to each tetrahedron element. The voxel is within a tetrahedron element only if all the corresponding barycentric coordinates (four in total) are nonnegative. If no tetrahedron element is available, we select the one closest to the voxel. After the corresponding tetrahedron element is localized for a voxel, the voxel's DVF can be obtained by weighting the DVFs of the four tetrahedron nodes using the barycentric coordinates. Accordingly, the biomechanical lung DVF defined on the tetrahedron nodes is converted to that defined on the image voxels.

After performing the conversion, the lung biomechanical DVF is merged with the intensity-based $v_{inverse}$ to replace the lung region in the latter. The resulting corrected DVF is iteratively fed back into the 2D-3D deformation until data fidelity-based stopping criteria are satisfied.

D. Evaluation materials: patient study

The efficacy of the Bio-CBCT-est technique was tested on eleven patients. Each analyzed patient has a 4D-CT set [20] acquired on a 16-slice Philips Brilliance CT scanner (Philips Medical Systems, Cleveland, Ohio). For each patient, ~80 anatomical landmarks were manually identified by a clinician for lung vascular and bronchial bifurcations, on both end-expiration (EE) and end-inspiration (EI) 4D-CT phase images to track lung motion. One of the selected lung biomarkers is shown in Figure 2. For each patient, ~40 biomarkers were marked in the middle of the lungs (~20 for the left lung and ~20 for the right lung). About 30 biomarkers were marked at the lung borders near the pleural region (~15 for the left lung and ~15 for the right lung). Another ~10 biomarkers were marked close to the tumor. In total, 872 landmarks were tracked for the eleven patients.

For each patient, the 4D-CT EE phase was used as the prior CT image for the deformation-based image estimation. The 4D-CT EI phase was used as the new image (the goal of estimation, also served as the 'ground-truth' volume for the estimation accuracy evaluation). Both EE and EI phase images were resampled to a voxel resolution of 1.5 mm* 1.5 mm* 1.5 mm. Based on the EI phase image, different numbers (5, 10, 20) of cone-beam projections spreading across a full 360° scan angle were simulated to represent different angular sampling sparseness. Each projection was simulated to have 300 * 250 pixels, with each pixel measuring 2 mm *2 mm in dimension.

To evaluate the effects of noise on the image estimation accuracy, various levels of imaging noise were also added to the simulated projections through (16):

$$P'_i = -\log_e \left(\frac{\text{Poisson} \left(I_0 e^{-P_i} \right) + \text{Normal} \left(0, \sigma^2 \right)}{I_0} \right) \quad (16)$$

The P'_i symbol indicates the noisy pixel value at location i . The I_0 symbol indicates the quantity of incident photons at each projection pixel. The P_i symbol indicates the noise-free line integral at pixel i . The *Poisson* term adds quantum noise to the projection based on its Poisson nature. The *Normal* term adds the electronic background noise in Gaussian form [7]. To simulate different noise levels, various I_0 values were used, including 10^4 , 10^5 , 10^6 and ∞ (noise-free). The σ^2 was kept constant at 10 and not included in the noise-free scenario.

E. Evaluation methods

To evaluate the accuracy of the deformed lung contour, which indicates the accuracy of the solved boundary condition for FEA, we can calculate the DICE coefficient [44] and the volume percentage error (VPE) [10] metric between the deformed lung contour (V_{Def}) and the ‘ground-truth’ lung contour (V_{GT}).

$$DICE = 2 * \frac{V_{Def} \cap V_{GT}}{V_{Def} + V_{GT}} \quad (17)$$

$$VPE = \frac{V_{Def} \cup V_{GT} - V_{Def} \cap V_{GT}}{V_{GT}} * 100\% \quad (18)$$

The *DICE* coefficient is a metric commonly used to evaluate how two contours match one another, with values ranging from 0 to 1. A larger *DICE* coefficient indicates a better match. Compared with the *DICE* coefficient, the *VPE* metric is more sensitive to the differences between two contours. A smaller *VPE* indicates a better match.

The estimated CBCT images were compared with the ‘ground-truth’ 4D-CT EI images to evaluate the estimation accuracy via the relative error (*RE*) metric.

$$RE = \sqrt{\frac{\sum (\mu_{est} - \mu_{GT})^2}{V}} \times 100\% \quad (19)$$

The μ_{est} symbol denotes the estimated CBCT volume’s voxel-wise attenuation coefficient. The μ_{GT} symbol denotes the ‘ground-truth’ volume’s voxel-wise attenuation coefficient.

The DVFs solved by the Bio-CBCT-est technique, representing the deformation between the EE and EI phases, were compared to the tracked landmark motion for accuracy evaluation. The residual error of DVF-tracked lung landmark motion (residual DVF error) is defined as:

$$\text{Residual DVF error} = \sqrt{\sum_{m=x,y,z} (v_m^{\text{Track}} - v_m^{\text{DVF}})^2} \quad (20)$$

The v^{Track} symbol denotes the manually-tracked landmark displacement vectors. The v^{DVF} symbol denotes the corresponding DVF-tracked landmark displacement vectors. The m parameter separates the displacement vectors into three canonical directions x , y , and z .

For comprehensive evaluation, the CBCT estimation accuracy of the Bio-CBCT-est technique was also compared to that of the 2D-3D deformation technique. Compared to Bio-CBCT-est, the 2D-3D deformation technique feeds the DVF solved from the previous iteration directly into the next iteration as a new starting point, without performing the FEA-based biomechanical modeling correction (Figure 1, steps 2–4). The two-sided Wilcoxon signed-rank test was performed between the results of the Bio-CBCT-est technique and the 2D-3D deformation technique. Statistical significance was defined at $p < 0.05$. In addition, the accuracy of the Bio-CBCT-est technique was also compared to that of the traditional Feldkamp-Davis-Kress (FDK) algorithm and the algebraic reconstruction technique with TV regularization (ART-TV).

III. Results

The tetrahedral mesh is generated from the 3D lung segmentation (Figure 4). The lung boundary conditions are extracted from 2D-3D deformation-generated DVFs (shown by the arrows on the surface of the tetrahedral mesh). The biomechanical DVF is then derived by FEA, based on the Mooney-Rivlin hyper-elastic model. In Figure 4, the FEA-derived biomechanical DVF is color-coded with hotter regions indicating larger deformations.

The DICE coefficients and VPEs of the deformed lung contours by the Bio-CBCT-est technique are shown in Table 1. Using 20 projections, the DICE coefficients for all the patients are >0.95 and the VPEs are $<10\%$. The results indicate that the 2D-3D deformation in Bio-CBCT-est has generated accurate boundary conditions for biomechanical modeling.

Figure 5 shows a comparison of estimated/reconstructed CBCT images between the FDK technique, the ART-TV technique, the 2D-3D deformation technique, and the Bio-CBCT-est technique. The FDK image presents severe streak artifacts with the use of only 10 projections for reconstruction. The ART-TV image removes the streak artifacts by TV regularization, but cannot recover the fine details in the lung due to under-sampling. The image estimated by 2D-3D deformation preserves the fine details from the prior image, which however mismatch with those in the ground-truth image due to incorrect DVF estimation. In comparison, Bio-CBCT-est not only preserves the fine details, but also successfully matches them to the ground-truth after biomechanical modeling.

A comparison of the lung DVFs generated from 2D-3D deformation and Bio-CBCT-est to the reference DVF is illustrated in Figure 6. The reference DVF was computed by directly registering the 4D-CT EE phase (prior image) to the 4D-CT EI phase (new image) by Demons registration [45]. The average residual error of the Demons DVF is 1.8 ± 1.3 mm as

evaluated by the manually-tracked lung landmark motion. The corresponding average residual DVF errors for the 2D-3D deformation technique and the Bio-CBCT-est technique are 4.6 ± 3.2 mm and 2.9 ± 2.4 mm, respectively. By visual comparison, the DVF of Bio-CBCT-est is more consistent with the Demons DVF as compared to that of 2D-3D deformation, especially in the regions with less contrast (far from the diaphragm).

The RE and the residual DVF error results are respectively reported in Tables 2 and 3. Statistical tests for both metrics show that the Bio-CBCT-est technique is significantly better ($p < 0.05$) than the 2D-3D deformation technique. The average residual DVF error is reduced by ~ 2 mm for all three projection number configurations (5, 10, 20), comparing the Bio-CBCT-est to the 2D-3D deformation technique (Table 3).

Image and DVF estimation results with noise introduced as (16) are reported in Table 4. The accuracy of the Bio-CBCT-est technique is slightly compromised (the RE increases by $\leq 1.04\%$ and the average residual DVF error increases by ≤ 0.4 mm) for the highest noise level (10^4 incident photons), which corresponds to a projection set noisier than normally observed in clinical scenarios (Figure 3).

IV. Discussion

A. Comparison between the Bio-CBCT-est technique and the 2D-3D deformation technique

The Bio-CBCT-est technique has achieved statistically significant ($p < 0.05$) improvement as compared to the 2D-3D deformation technique (Table 2, Table 3), especially in terms of DVF accuracy (Table 3). For the Bio-CBCT-est technique, an average residual DVF error within 3.5 mm can be achieved by using only 5 projections for estimation. The results suggest that combining biomechanical modeling with 2D-3D deformation achieves more accurate DVFs. The biomechanical modeling uses geometric/elastic properties of the anatomical structures, which can be viewed as additional constraints that helped guide the DVF optimization. Since FEA derives the biomechanical DVFs through considering each tetrahedral element in the structure mesh, this also helps correct the erroneous DVFs in the low-contrast regions not well deformed by the intensity-based 2D-3D deformation technique. The corrected low-contrast regions could, in turn, help to improve the DVFs in the high-contrast regions through the iterative approach of the Bio-CBCT-est technique. Previous studies tried to combine the intensity-based deformation techniques with biomechanical modeling to improve 3D image registration accuracy and generated improved results [21], [25]. Our work is the first to combine 2D-3D deformation with biomechanical modeling for CBCT estimation, leading to encouraging results (Figure 5, Figure 6, Table 2, Table 3).

The superiority of Bio-CBCT-est over the 2D-3D deformation technique on RE reduction is less prominent, as compared to that on residual DVF error reduction. Bio-CBCT-est further reduces the average RE by 0.51% – 1.65% (Table 2) as compared to 2D-3D deformation. In contrast, Bio-CBCT-est further reduces the average residual DVF error by 1.9 mm – 2.5 mm (Table 3) compared to 2D-3D deformation. The effect of RE reduction is less prominent, because the Bio-CBCT-est technique primarily benefits from more accurate deformation at low-contrast regions with fine structures and small intensity differences, and the low-

contrast regions' contribution to the intensity-based RE metric is limited. However, low REs do not necessarily guarantee high-quality motion estimation. The DVFs can be incorrect (Table 3) even with a low RE, leading to substantial errors if the solved DVFs are used for motion tracking or treatment dose deformation/accumulation in radiation therapy, especially around the low-contrast areas [46]. Thus the DVF accuracy improvement achieved in this study is of clinical relevance in the practice of radiotherapy. DVF-based lung ventilation imaging is also highly sensitive to DVF accuracy [47]; this is another area that may potentially benefit from the development of Bio-CBCT-est.

B. Comparisons with previous relevant studies

A previous study that used the same patient sample as ours yielded an average residual DVF error of ~3.3 mm [20], slightly higher than what we obtained in this study (2.9 mm average residual DVF error by using 20 projections). Compared with this previous publication, which is based on pure biomechanical modeling, the Bio-CBCT-est technique mainly benefits from the advantage of combining intensity-based 2D-3D deformation and biomechanical modeling. The boundary conditions in the aforementioned previous study are well-defined as they are directly extracted from high quality CT images. In contrast, Bio-CBCT-est obtains boundary conditions only from limited-view 2D projections, validating the accuracy of the boundary condition recovery through 2D-3D deformation (Table 1).

Another study [48] developed a 'navigator channel'-based approach to reconstruct 3D lung models from 2D planning projections. Compared with the 'navigator channel' based technique, Bio-CBCT-est does not require a library of patients to build a pool of lung models. Bio-CBCT-est also does not need the error-prone model morphing process from patient to patient. Bio-CBCT-est uses the 2D-3D deformation technique to solve the lung boundary condition. The 2D-3D deformation technique also solves the deformation field for structures outside the lung. In contrast, the 'navigator channel' technique updates the DVF based on a limited scope of selected anatomical landmarks and can only solve the DVF inside the lung.

C. Computational cost of the algorithm

The implementation of the Bio-CBCT-est algorithm is currently semi-automatic, except for the manual lung segmentation fine-tuning process. Manual fine-tuning involves limited labor efforts, since the lung boundary is high-contrast and automatic segmentation methods are generally very effective. The three steps, including the semi-automatic lung segmentation, the tetrahedral mesh generation, and the barycentric coordinates computation, can be completed in less than 1 hour combined. The three steps are 'off-line' and can be conducted any time after the high-quality prior image is obtained. The 'on-line' steps (2D-3D deformation + FEA), enforced after the 2D projections are acquired, generally require 1–2 hours, by using 5–20 projections for image estimation. In detail, each 2D-3D deformation step takes 3–5 minutes for 5–20 projections, and each FEA step takes less than 30 seconds. The algorithm converges in 10–15 iterations for all the studied cases.

The above computation speed is based on a personal computer with a 3.6 GHz Intel Core i7-4790 CPU and an NVIDIA Quadro K4200 GPU. For the current code implementation,

we include only a preliminary GPU acceleration scheme for the forward and backward projection steps within each projection view, due to the limited memory of the GPU card. The computation of the algorithm can be further accelerated by implementing a full GPU acceleration scheme within the total projection set. A GPU parallelization for the line-search step used in the nonlinear conjugate gradient descent process is also expected to further accelerate the Bio-CBCT-est algorithm. In addition to GPU acceleration, there is also potential to modify the code to enable multi-threading on the CPU to further accelerate the computation speed of the algorithm.

D. Potential improvements/limitations of the current Bio-CBCT-est technique

In this study, the lung is modeled as an isotropic, homogeneous organ with the same elasticity parameters. In reality, biomechanical parameters can vary among different lung lobes, and between the lung and the tumor. The elasticity parameters can also differ between the parenchyma, the lung vessels, and the bronchial trees. Though previous studies validated the accuracy and efficacy of modeling the lung as a whole homogeneous organ [18], [20], further studies are warranted to investigate the potential benefits of exploring lung heterogeneity [22], [23] and further improve the estimation accuracy. In addition, biomechanical modeling of other structures, including the spine, the ribs, and the chest wall, may also help to further improve image estimation accuracy. We can also potentially model the sliding motion between the chest wall and the lung by prescribing the boundary condition to the adjacent chest wall (instead of the lung surface itself) and allowing the lung to slide along the chest wall boundary. This approach has generated better results [19], [26] than that without considering sliding motion. In the current study, the DVF accuracy was only evaluated in the lung. The accuracy of structures outside of lung was only implicitly evaluated by the RE metric. The deformation field accuracy of these structures can be evaluated by tracking anatomical landmarks within each of them individually.

We use a fast symmetric term-based optimization strategy to solve the inverse deformation field (6). During optimization, the inverse DVF is viewed as the negative of the forward DVF, a simple and straightforward approach validated in previous studies [8], [31]. Other deformation field inversion techniques, including the scatter data interpolation, the Newton's method [32], and the fixed-point approach [33], may also be potential candidates although more complex and time-consuming.

In this study, the end-expiration phase of 4D-CT is used as the high-quality prior volume for biomechanical modeling. The end-expiration phase is usually the most stable and reproducible phase with limited motion artifacts [49]. In cases of patients with very irregular breathing, the quality of 4D-CT may be compromised with severe motion artifacts. These extreme scenarios are not observed in the patient samples of this study. In clinical practice, if prominent irregularities exist, patients can be assisted with breathing coaching [50] or compression devices to make the breathing pattern more reproducible. A detailed analysis taking breathing irregularities into account will be performed on a larger patient cohort in the future.

We simulated cone-beam projections from the CT images to evaluate the efficacy of our algorithm, since high quality CT images can provide a 'ground-truth' for reference. A

preliminary robustness study was also performed to evaluate the accuracy of our technique when different levels of noise exist (Table 4). Other nonlinearity factors observed in clinical cone-beam projections, including the scatter and the imager lags, are not included in the cone-beam projection simulation. These factors may affect the accuracy of the proposed estimation algorithm, especially when CT images are used as the prior information for CBCT estimation (CBCT projections present more scatters than CT). Previous studies investigated multiple scatter correction/reduction techniques and achieved encouraging results [28], [51], [52]. The imager lags can also be corrected by using a measurement-based approach [53]. More robust image similarity metrics, including the normalized cross-correlation [10] and the mutual information, can also be used to replace the sum of squared differences metric used in this study for better robustness against the intensity variations between the CT and CBCT systems. The effects of these nonlinearity factors and the aforementioned solutions will be investigated with clinically-measured data. The clinical study requires both high-quality 4D-CT for image estimation and fully-sampled high-quality 4D-CBCT images to evaluate the quality of estimated lung phase images by Bio-CBCT-est, especially when evaluating the accuracy of the fine lung details. The corresponding clinical evaluation results will be reported in a future study once the patient data are available.

In this study, the new CBCTs were estimated from prior CT/CBCT images using a deformation-based approach. In some scenarios, non-deformation-induced intensity changes may exist, including necrosis or inflammation. These non-deformation components will not be recovered by the deformation-based approach. We have previously developed a simultaneous motion estimation and image reconstruction technique (SMEIR) [34] to combine motion estimation with a motion-corrected simultaneous algebraic reconstruction technique for 4D-CBCT reconstruction. We are currently extending our biomechanical modeling-based method to SMEIR, which can recover these non-deformation-induced changes. Another solution to these non-deformation-induced intensity change problems is to acquire new fully-sampled CT/CBCT images periodically during the treatment course, which will incorporate these non-deformation-induced intensity changes into a new prior image. For these non-deformation-induced intensity changes difficult to recover by deformation alone, the data fidelity error will notably increase even with converged optimization; this can potentially remind clinicians that a new fully-sampled CT/CBCT scan is needed to replace the current prior image.

Another potential limitation of our technique is that its accuracy may potentially be limited in structures with poorly defined boundaries (e.g. some prostate cases). A previous publication by Brock et. al proposed the use of ‘implicit boundary conditions’ [18] that are implicitly determined by the boundary conditions of neighboring organs (e.g. bladder and rectum for the prostate cases) for biomechanical modeling. Encouraging results have been achieved. The efficacy of this method, however, is pending further investigation for our algorithm.

In summary, potential improvements can be made to increase the accuracy of our technique. Factors including motion irregularity and imaging system differences (for instance, different scatter and imager lag pattern) also need to be investigated to evaluate their effects on the accuracy of the algorithm. Although we estimated CBCT images from prior CT images in

this study, our method can be readily applied to estimate CT from prior CT images or CBCT from prior CBCT images, where the intensity mismatch caused by imaging system differences will be greatly reduced. Our method can also be applied to other imaging sites where periodic motion may not be involved.

E. Future prospects

We evaluated the accuracy of the developed Bio-CBCT-est technique using eleven lung cancer patient cases. The Bio-CBCT-est technique is readily applicable to image estimation at other anatomical sites, such as the head and neck, the liver, and the pelvis. The technique is especially promising for low-contrast abdominal sites including the liver, since the low soft-tissue contrast within this organ impedes accurate intensity-based 2D-3D deformation [5]. Relevant work is currently in progress and will be reported as a follow-up study.

V. Conclusion

The Bio-CBCT-est technique improves the accuracy of the estimated images and the corresponding DVFs, demonstrating the advantages of incorporating material biomechanical properties into DVF optimization and image estimation. The resulting accurate DVFs can be applied in several areas of radiation therapy, including structure tracking/localization, dose accumulation, and adaptive radiation therapy.

Supplementary Material

Refer to Web version on PubMed Central for supplementary material.

Acknowledgments

We acknowledge funding support from the American Cancer Society (RSG-13-326-01-CCE), from the US National Institutes of Health (R01 EB020366), and from the Cancer Prevention and Research Institute of Texas (RP130109).

The authors would like to thank Dr. Zichun Zhong at the Wayne State University for his help with barycentric coordinate computation. The authors would also like to thank Dr. Rene Werner at the University Medical Center Hamburg-Eppendorf, Dr. Wei Lu at the University of Maryland, and Dr. Daniel Low at the University of California, Los Angeles for sharing patient data. The authors would also like to thank Dr. Damiana Chiavolini at the UT Southwestern Medical Center at Dallas for editing the paper.

References

1. Xing L, et al. Overview of image-guided radiation therapy. *Med Dosim.* Summer;2006 31:91–112. [PubMed: 16690451]
2. Kim DW, Chung WK, Yoon M. Imaging doses and secondary cancer risk from kilovoltage cone-beam CT in radiation therapy. *Health Phys.* May.2013 104:499–503. [PubMed: 23532078]
3. Zeng R, Fessler JA, Balter JM. Estimating 3-D respiratory motion from orbiting views by tomographic image registration. *IEEE Trans Med Imaging.* Feb.2007 26:153–63. [PubMed: 17304730]
4. Li R, et al. Real-time volumetric image reconstruction and 3D tumor localization based on a single x-ray projection image for lung cancer radiotherapy. *Med Phys.* Jun.2010 37:2822–6. [PubMed: 20632593]
5. Ren L, et al. Development and clinical evaluation of a three-dimensional cone-beam computed tomography estimation method using a deformation field map. *Int J Radiat Oncol Biol Phys.* Apr 1.2012 82:1584–93. [PubMed: 21477945]

6. Zhang Y, Yin FF, Segars WP, Ren L. A technique for estimating 4D-CBCT using prior knowledge and limited-angle projections. *Med Phys.* Dec.2013 40:121701. [PubMed: 24320487]
7. Wang J, Gu X. High-quality four-dimensional cone-beam CT by deforming prior images. *Phys Med Biol.* Jan 21.2013 58:231–46. [PubMed: 23257113]
8. Wang J, Gu X. Simultaneous Motion Estimation and Image Reconstruction (SMEIR) for 4D Cone-Beam CT. *Medical Physics.* Jun.2013 40
9. Flach B, Brehm M, Sawall S, Kachelriess M. Deformable 3D-2D registration for CT and its application to low dose tomographic fluoroscopy. *Phys Med Biol.* Dec 21.2014 59:7865–87. [PubMed: 25426660]
10. Zhang Y, Yin FF, Pan T, Vergalasova I, Ren L. Preliminary clinical evaluation of a 4D-CBCT estimation technique using prior information and limited-angle projections. *Radiother Oncol.* Apr. 2015 115:22–9. [PubMed: 25818396]
11. Cai W, et al. 3D delivered dose assessment using a 4DCT-based motion model. *Med Phys.* Jun. 2015 42:2897–907. [PubMed: 26127043]
12. Zhang Y, Yin FF, Ren L. Dosimetric verification of lung cancer treatment using the CBCTs estimated from limited-angle onboard projections. *Med Phys.* Aug.2015 42:4783–95. [PubMed: 26233206]
13. Keall PJ, Joshi S, Vedam SS, Siebers JV, Kini VR, Mohan R. Four-dimensional radiotherapy planning for DMLC-based respiratory motion tracking. *Med Phys.* Apr.2005 32:942–51. [PubMed: 15895577]
14. Thor M, et al. Evaluation of an application for intensity-based deformable image registration and dose accumulation in radiotherapy. *Acta Oncol.* Oct.2014 53:1329–36. [PubMed: 24957554]
15. Wu QJ, Li T, Wu Q, Yin FF. Adaptive radiation therapy: technical components and clinical applications. *Cancer J.* May-Jun;2011 17:182–9. [PubMed: 21610472]
16. Castillo R, Castillo E, Martinez J, Guerrero T. Ventilation from four-dimensional computed tomography: density versus Jacobian methods. *Phys Med Biol.* Aug 21.2010 55:4661–85. [PubMed: 20671351]
17. Tehrani JN, et al. Sensitivity of tumor motion simulation accuracy to lung biomechanical modeling approaches and parameters. *Phys Med Biol.* Nov 21.2015 60:8833–49. [PubMed: 26531324]
18. Brock KK, Sharpe MB, Dawson LA, Kim SM, Jaffray DA. Accuracy of finite element model-based multi-organ deformable image registration. *Med Phys.* Jun.2005 32:1647–59. [PubMed: 16013724]
19. Al-Mayah A, Moseley J, Brock KK. Contact surface and material nonlinearity modeling of human lungs. *Phys Med Biol.* Jan 7.2008 53:305–17. [PubMed: 18182705]
20. Werner R, Ehrhardt J, Schmidt R, Handels H. Patient-specific finite element modeling of respiratory lung motion using 4D CT image data. *Med Phys.* May.2009 36:1500–11. [PubMed: 19544766]
21. Zhong H, Kim J, Li H, Nurusev T, Movsas B, Chetty IJ. A finite element method to correct deformable image registration errors in low-contrast regions. *Phys Med Biol.* Jun 7.2012 57:3499–515. [PubMed: 22581269]
22. Li M, et al. Modeling lung deformation: a combined deformable image registration method with spatially varying Young's modulus estimates. *Med Phys.* Aug.2013 40:081902. [PubMed: 23927316]
23. Nasehi Tehrani J, Wang J. Mooney-Rivlin biomechanical modeling of lung with Inhomogeneous material. *Conf Proc IEEE Eng Med Biol Soc.* Aug.2015 2015:7897–900. [PubMed: 26738123]
24. Zhang T, Orton NP, Mackie TR, Paliwal BR. Technical note: A novel boundary condition using contact elements for finite element based deformable image registration. *Med Phys.* Sep.2004 31:2412–5. [PubMed: 15487720]
25. Samavati N, Velec M, Brock K. A hybrid biomechanical intensity based deformable image registration of lung 4DCT. *Phys Med Biol.* Apr 21.2015 60:3359–73. [PubMed: 25830808]
26. Al-Mayah A, Moseley J, Velec M, Brock KK. Sliding characteristic and material compressibility of human lung: parametric study and verification. *Med Phys.* Oct.2009 36:4625–33. [PubMed: 19928094]

27. Feldkamp LA, Davis LC, Kress JW. Practical Cone-Beam Algorithm. *Journal of the Optical Society of America a-Optics Image Science and Vision*. 1984; 1:612–619.
28. Wang J, Mao W, Solberg T. Scatter correction for cone-beam computed tomography using moving blocker strips: a preliminary study. *Med Phys*. Nov.2010 37:5792–800. [PubMed: 21158291]
29. Sotiras A, Davatzikos C, Paragios N. Deformable medical image registration: a survey. *IEEE Trans Med Imaging*. Jul.2013 32:1153–90. [PubMed: 23739795]
30. Lu W, Chen ML, Olivera GH, Ruchala KJ, Mackie TR. Fast free-form deformable registration via calculus of variations. *Phys Med Biol*. Jul 21.2004 49:3067–87. [PubMed: 15357182]
31. Yang D, Li H, Low DA, Deasy JO, El Naqa I. A fast inverse consistent deformable image registration method based on symmetric optical flow computation. *Phys Med Biol*. Nov 7.2008 53:6143–65. [PubMed: 18854610]
32. Gobbi DG, Peters TM. Generalized 3D nonlinear transformations for medical imaging: an object-oriented implementation in VTK. *Comput Med Imaging Graph*. Jul-Aug;2003 27:255–65. [PubMed: 12631510]
33. Chen M, Lu W, Chen Q, Ruchala KJ, Olivera GH. A simple fixed-point approach to invert a deformation field. *Med Phys*. Jan.2008 35:81–8. [PubMed: 18293565]
34. Wang J, Gu X. Simultaneous motion estimation and image reconstruction (SMEIR) for 4D cone-beam CT. *Med Phys*. Oct.2013 40:101912. [PubMed: 24089914]
35. Mooney M. A theory of large elastic deformation. *Journal of Applied Physics*. Sep.1940 11:582–592.
36. Skrinjar O, Nabavi A, Duncan J. Model-driven brain shift compensation. *Med Image Anal*. Dec. 2002 6:361–73. [PubMed: 12494947]
37. Paragios, N., Duncan, J., Ayache, N. *Handbook of Biomedical Imaging: Methodologies and Clinical Research*. Vol. 779. Springer; 2015.
38. Sundaram TA, Gee JC. Towards a model of lung biomechanics: pulmonary kinematics via registration of serial lung images. *Med Image Anal*. Dec.2005 9:524–37. [PubMed: 15896996]
39. Yushkevich PA, et al. User-guided 3D active contour segmentation of anatomical structures: significantly improved efficiency and reliability. *Neuroimage*. Jul 1.2006 31:1116–28. [PubMed: 16545965]
40. Fang, QQ., Boas, DA. Tetrahedral Mesh Generation from Volumetric Binary and Gray-Scale Images. 2009 *Ieee International Symposium on Biomedical Imaging: From Nano to Macros 1 and 2*; 2009. p. 1142-1145.
41. Si H. TetGen, a Delaunay-Based Quality Tetrahedral Mesh Generator. *Acm Transactions on Mathematical Software*. Jan.2015 41
42. Maas SA, Ellis BJ, Ateshian GA, Weiss JA. FEBio: finite elements for biomechanics. *J Biomech Eng*. Jan.2012 134:011005. [PubMed: 22482660]
43. Zhong Z, Gu X, Mao W, Wang J. 4D cone-beam CT reconstruction using multi-organ meshes for sliding motion modeling. *Physics in medicine and biology*. 2016; 61:996. [PubMed: 26758496]
44. Fotina I, Lutendorf-Caucig C, Stock M, Potter R, Georg D. Critical discussion of evaluation parameters for inter-observer variability in target definition for radiation therapy. *Strahlenther Onkol*. Feb.2012 188:160–7. [PubMed: 22281878]
45. Gu X, et al. Implementation and evaluation of various demons deformable image registration algorithms on a GPU. *Phys Med Biol*. Jan 7.2010 55:207–19. [PubMed: 20009197]
46. Juang T, Das S, Adamovics J, Benning R, Oldham M. On the need for comprehensive validation of deformable image registration, investigated with a novel 3-dimensional deformable dosimeter. *Int J Radiat Oncol Biol Phys*. Oct 1.2013 87:414–21. [PubMed: 23886417]
47. Latifi K, et al. Effects of quantum noise in 4D-CT on deformable image registration and derived ventilation data. *Phys Med Biol*. Nov 7.2013 58:7661–72. [PubMed: 24113375]
48. Ng A, Nguyen TN, Moseley JL, Hodgson DC, Sharpe MB, Brock KK. Reconstruction of 3D lung models from 2D planning data sets for Hodgkin's lymphoma patients using combined deformable image registration and navigator channels. *Med Phys*. Mar.2010 37:1017–28. [PubMed: 20384237]

49. Seppenwoolde Y, et al. Precise and real-time measurement of 3D tumor motion in lung due to breathing and heartbeat, measured during radiotherapy. *Int J Radiat Oncol Biol Phys.* Jul 15.2002 53:822–34. [PubMed: 12095547]
50. Pollock S, Keall R, Keall P. Breathing guidance in radiation oncology and radiology: A systematic review of patient and healthy volunteer studies. *Med Phys.* Sep.2015 42:5490–509. [PubMed: 26328997]
51. Ren L, Chen Y, Zhang Y, Giles W, Jin J, Yin FF. Scatter Reduction and Correction for Dual-Source Cone-Beam CT Using Prepatient Grids. *Technol Cancer Res Treat.* May 24.2015
52. Xu Y, et al. A practical cone-beam CT scatter correction method with optimized Monte Carlo simulations for image-guided radiation therapy. *Phys Med Biol.* May 7.2015 60:3567–87. [PubMed: 25860299]
53. Hsieh J, Gurmen OE, King KF. A recursive correction algorithm for detector decay characteristics in CT. *Medical Imaging 2000: Physics of Medical Imaging.* 2000; 3977:298–305.

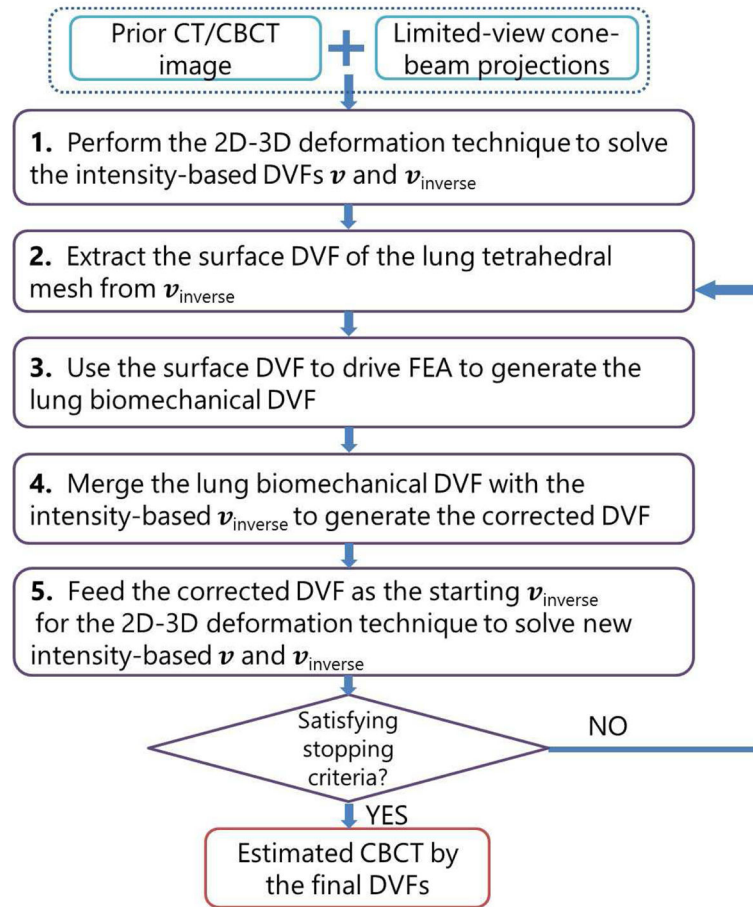


Fig. 1.
Work-flow of the Bio-CBCT-est technique.



Fig. 2.
An example of a bifurcation identified by the clinician as a lung landmark.

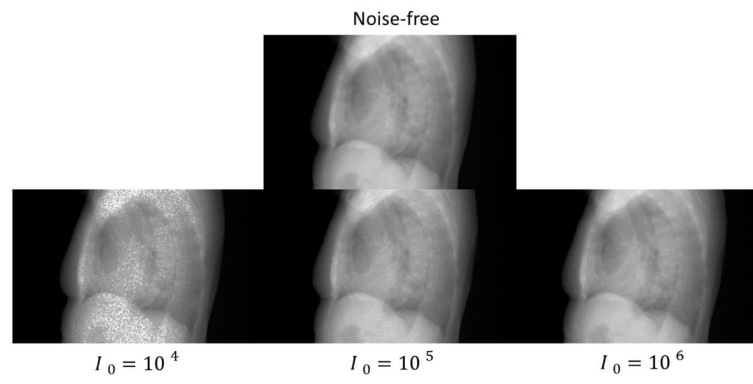


Fig. 3. Simulated projections showing different levels of incorporated noise. The quantum noise increases as I_0 decreases.

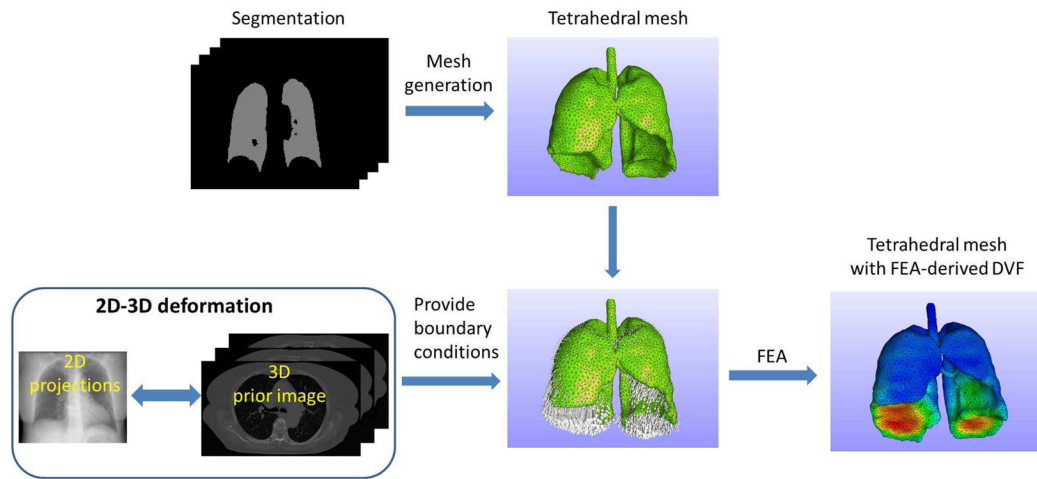


Fig. 4.
Work-flow of the lung biomechanical modeling process.

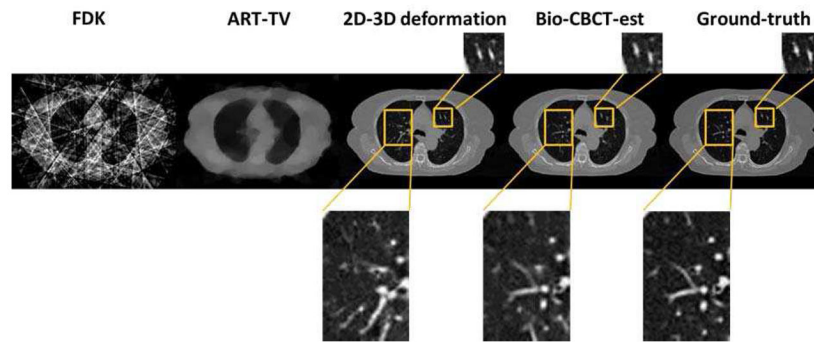


Fig. 5.

Axial slice cuts of the reconstructed CBCT by the FDK algorithm, the reconstructed CBCT by the ART-TV algorithm., the estimated CBCT by the 2D-3D deformation technique, the estimated CBCT by the Bio-CBCT-est technique, and the ‘ground-truth’ 4D-CT EI image. The magnified images show the fine details of the lung. The display window is $[0, 0.08 \text{ mm}^{-1}]$ for the original images and $[0, 0.04 \text{ mm}^{-1}]$ for the enlarged images. The figure corresponds to patient 04, by using 10 projections for CBCT reconstruction/estimation.

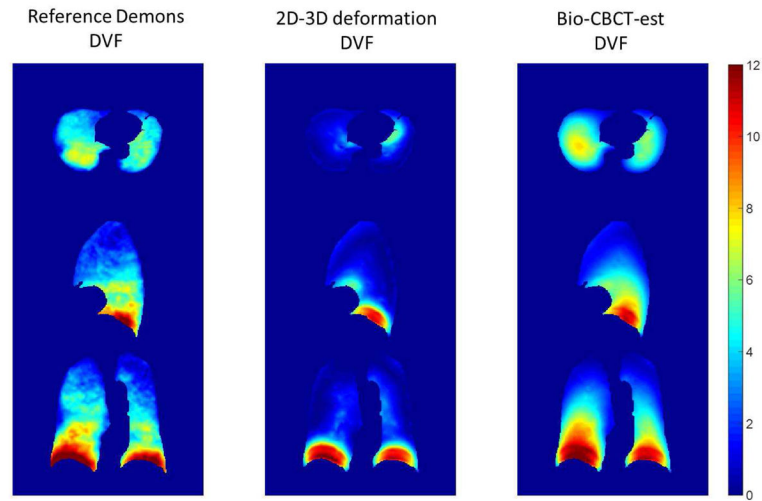


Fig. 6. Comparison between three DVFs: the reference lung DVF computed from Demons registration, the lung DVF computed from 2D-3D deformation, and the lung DVF computed from Bio-CBCT-est. The color bar on the right denotes the vector magnitudes of the deformation (unit: mm).

DICE coefficients and VPEs of the deformed lung contours by the Bio-CBCCT-est technique for all the studied patients, using different number of projections. The 'prior' column shows the DICE coefficients and VPEs of the prior lung contours (at the EE phase).

TABLE I

Patients	Metrics	Prior	5 proj	10 proj	20 proj
P01	DICE	0.901	0.946	0.959	0.965
	VPE	18.38%	10.75%	8.30%	7.08%
P02	DICE	0.905	0.944	0.951	0.958
	VPE	17.48%	11.30%	9.98%	8.56%
P03	DICE	0.897	0.959	0.965	0.969
	VPE	19.17%	8.27%	7.04%	6.21%
P04	DICE	0.913	0.957	0.969	0.977
	VPE	16.42%	8.38%	6.11%	4.68%
P05	DICE	0.879	0.935	0.952	0.964
	VPE	22.15%	12.56%	9.40%	7.08%
P06	DICE	0.902	0.958	0.964	0.970
	VPE	18.17%	8.19%	7.13%	6.01%
P07	DICE	0.884	0.946	0.959	0.966
	VPE	21.23%	10.69%	8.21%	6.84%
P08	DICE	0.941	0.968	0.972	0.975
	VPE	11.37%	6.49%	5.69%	5.18%
P09	DICE	0.949	0.974	0.977	0.979
	VPE	9.96%	5.25%	4.60%	4.20%
P10	DICE	0.863	0.920	0.939	0.954
	VPE	24.58%	15.45%	12.04%	9.21%
P11	DICE	0.899	0.947	0.953	0.961
	VPE	18.88%	10.65%	9.50%	8.02%

TABLE II

Relative errors (RE) of the reconstructed/estimated CBCT images when compared to the 'ground-truth' 4D-CT EI phase image of each patient. The results are based on different angular sampling sparseness (by using different numbers of projections). The symbol '**' indicates that a statistically significant difference ($p < 0.05$) was observed between the REs of the 2D-3D deformation technique and the Bio-CBCT-est technique.

Patients	RE (%) after CBCT estimation/reconstruction											
	5 projection				10 projection				20 projection			
	FDK	ART-TV	2D-3D Deformation	Bio-CBCT-est	FDK	ART-TV	2D-3D Deformation	Bio-CBCT-est	FDK	ART-TV	2D-3D Deformation	Bio-CBCT-est
P01	57.87	25.23	11.15	11.19	40.47	16.05	10.31	9.62	29.18	10.96	9.19	8.60
P02	64.27	28.96	13.60	13.97	43.74	16.70	13.55	12.01	31.51	11.39	10.07	10.10
P03	59.16	25.17	10.67	9.55	44.69	14.63	10.20	8.52	36.64	10.97	8.22	7.76
P04	72.08	29.66	15.87	12.77	48.71	18.79	14.06	10.45	32.38	12.61	9.46	8.92
P05	70.86	28.87	13.81	13.69	51.05	19.24	11.31	11.11	36.95	13.45	9.51	9.25
P06	67.22	26.44	9.21	8.97	46.44	17.27	8.63	8.07	33.40	12.29	7.14	7.17
P07	59.09	26.43	13.41	11.23	40.19	16.65	10.17	9.17	28.63	11.36	8.70	7.89
P08	79.13	36.27	16.06	14.40	55.41	22.44	15.59	11.50	37.38	14.05	9.95	9.46
P09	85.27	32.88	11.65	11.62	58.21	21.32	10.39	10.50	42.37	15.34	9.35	9.51
P10	60.91	25.26	17.02	14.63	41.69	16.72	15.76	12.22	31.61	10.84	12.06	9.99
P11	60.59	27.39	13.03	12.94	40.74	16.41	12.45	11.07	29.96	11.36	10.01	9.34
Average \pm S.D.	66.95 \pm 8.61	28.41 \pm 3.35	13.23 \pm 2.32	12.27 \pm 1.83*	46.49 \pm 5.92	17.84 \pm 2.26	12.04 \pm 2.29	10.39 \pm 1.32*	33.64 \pm 4.03	12.24 \pm 1.41	9.42 \pm 1.18	8.91 \pm 0.91*

(Average \pm S.D.) Residual DVF errors for each patient by using manually-tracked lung landmark motion as the 'ground-truth'. The results are based on different angular sampling sparseness (by using different numbers of projections) and different estimation methods. 'Landmark motion' shows the (Average \pm S.D.) motion amplitude of the lung landmarks manually tracked between the prior image (4D-CT EE phase) and the 'ground-truth' new image (4D-CT EI phase), which is also the residual error of a zero DVF. The symbol '*' indicates that a statistically significant difference ($p < 0.05$) was observed between the residual DVF error results of the 2D-3D deformation technique and the Bio-CBCT-est technique. Note that the statistical tests were performed on the results of each patient and also on the cumulative results of all 11 patients.

TABLE III

Patients	Landmark Motion (mm)	(Average \pm S.D.) Residual DVF errors (mm) after CBCT estimation					
		5 projection		10 projection		20 projection	
		2D-3D Deformation	Bio-CBCT-est	2D-3D Deformation	Bio-CBCT-est	2D-3D Deformation	Bio-CBCT-est
P01	6.4 \pm 3.1	5.5 \pm 2.1	3.6 \pm 1.9*	5.5 \pm 2.1	2.9 \pm 1.6*	5.4 \pm 2.1	2.7 \pm 1.4*
P02	6.2 \pm 6.9	5.3 \pm 5.6	3.9 \pm 4.1*	5.7 \pm 6.1	3.4 \pm 3.4*	4.8 \pm 5.1	3.0 \pm 2.7*
P03	6.8 \pm 3.8	5.6 \pm 3.3	3.0 \pm 1.9*	5.9 \pm 3.5	2.7 \pm 1.6*	4.8 \pm 3.1	2.7 \pm 1.5*
P04	6.3 \pm 4.8	5.8 \pm 4.3	3.7 \pm 3.0*	5.7 \pm 4.2	3.2 \pm 2.7*	4.6 \pm 3.2	2.9 \pm 2.4*
P05	5.4 \pm 2.7	4.6 \pm 2.4	3.3 \pm 1.9*	4.3 \pm 2.3	3.0 \pm 1.7*	3.7 \pm 2.3	2.6 \pm 1.5*
P06	6.2 \pm 2.2	4.7 \pm 1.4	2.8 \pm 1.4*	5.2 \pm 1.6	2.8 \pm 1.4*	3.9 \pm 1.6	2.7 \pm 1.5*
P07	4.3 \pm 3.2	4.0 \pm 2.6	2.8 \pm 1.7*	3.6 \pm 2.4	2.8 \pm 1.8*	3.5 \pm 2.4	2.8 \pm 2.0*
P08	6.1 \pm 5.1	5.4 \pm 4.3	3.4 \pm 2.3*	5.4 \pm 4.4	3.0 \pm 2.0*	4.1 \pm 3.6	2.8 \pm 1.9*
P09	4.3 \pm 2.6	3.4 \pm 2.1	2.0 \pm 1.4*	3.2 \pm 2.1	1.9 \pm 1.3*	2.8 \pm 2.0	1.7 \pm 1.2*
P10	8.3 \pm 6.4	7.8 \pm 5.8	4.9 \pm 4.2*	7.6 \pm 5.6	4.2 \pm 3.4*	6.8 \pm 4.9	3.7 \pm 3.0*
P11	10.8 \pm 7.8	8.1 \pm 5.3	5.1 \pm 3.8*	8.6 \pm 5.8	4.5 \pm 3.2*	7.8 \pm 5.3	3.8 \pm 2.7*
Average \pm S.D. (for all 11 patients)		6.5 \pm 5.1	3.5 \pm 2.9*	5.6 \pm 4.3	3.1 \pm 2.4*	4.8 \pm 3.8	2.9 \pm 2.1*

TABLE IV

Relative errors (RE) and residual DVF errors after Bio-CBCT-est based estimation for patient 04, with regard to different noise levels (by using different numbers of incident photons).

Incident photons	RE (%) after Bio-CBCT-est		
	5 projection	10 projection	20 projection
1e4	12.95	10.94	9.96
1e5	12.77	10.38	8.85
1e6	12.77	10.45	8.92
Noise-free	12.77	10.45	8.92

Incident photons	(Average \pm S.D.) Residual DVF errors (mm) after Bio-CBCT-est		
	5 projection	10 projection	20 projection
1e4	3.9 \pm 3.2	3.3 \pm 2.7	3.3 \pm 2.7
1e5	3.7 \pm 3.0	3.2 \pm 2.6	2.8 \pm 2.3
1e6	3.7 \pm 3.0	3.2 \pm 2.7	2.9 \pm 2.4
Noise-free	3.7 \pm 3.0	3.2 \pm 2.7	2.9 \pm 2.4